minerals

MDPI

Article

Authigenic Fe Mineralization in Shallow to Marginal Marine Environments: A Case Study from the Late Paleocene—Early Eocene Cambay Shale Formation

Tathagata Roy Choudhury [1], Pragya Singh [2], Arpita Chakraborty [2] and Santanu Banerjee [2,*]

[1] Department of Geological Sciences, Jadavpur University, Kolkata 700032, West Bengal, India
[2] Department of Earth Sciences, Indian Institute of Technology Bombay, Powai, Mumbai 400076, Maharashtra, India
* Correspondence: santanu@iitb.ac.in

Abstract: The late Paleocene–early Eocene warm greenhouse conditions, characterized by elevated pCO_2 levels in the atmosphere and a dramatic increase in sea surface temperature, prompted abundant authigenic glauconite formation within the shallow marine sediments worldwide by lowering the net sedimentation rate, increasing organic productivity and expanding the oxygen minimum zones to shallow oceans. The early Eocene marginal marine Cambay Shale Formation experienced episodes of marine inundation represented by limestone–green shale alternations. The shales host abundant authigenic light-green, dark-green, and brown pellets. A detailed characterization of the pellets of the Valia and Vastan lignite mines, integrating the sedimentological, petrographical, mineralogical, and mineral geochemical data, suggests two distinct varieties of Fe–silicate formation, viz. glauconite and chamosite. While the glauconitic green pellets are ubiquitous to Valia and Vastan mines, brown chamosite pellets are confined within the basal part of the green shale facies alternating with fossiliferous limestone in the Vastan mine. The glauconites of the Valia mine manifest a 'nascent' to 'slightly evolved' maturation stage of glauconitization, whereas the glauconites of the Vastan mine represent the 'evolved' type. The limestone–green shale alternation in the Valia mine is overlain by a ~4 m-thick spherulitic mudstone facies comprising monomineralic sideritic spherulites, reflecting a pure $FeCO_3$ composition. The glauconites in the Cambay Shale Formation transformed from kaolinite-rich clay pellets under dys-oxic depositional conditions. The increasing anoxicity within the microenvironment, possibly amplified by the rapid oxidation of continent-derived organic matter, facilitated chamosite formation instead of glauconite. The increased freshwater influx into the marginal marine depositional environment resulted in immature, K-poor glauconites of the Valia mine. The formation of siderite spherulites overlying the limestone–green shale alternation relates to the beginning of the regressive phase of sedimentation.

Keywords: glauconite; chamosite; siderite; early Eocene; warm climate; Cambay Basin

check for updates

Citation: Roy Choudhury, T.; Singh, P.; Chakraborty, A.; Banerjee, S. Authigenic Fe Mineralization in Shallow to Marginal Marine Environments: A Case Study from the Late Paleocene—Early Eocene Cambay Shale Formation. *Minerals* **2023**, *13*, 646. https://doi.org/10.3390/min13050646

Academic Editors: Javier Sánchez-España and Pierre Giresse

Received: 28 January 2023
Revised: 27 March 2023
Accepted: 5 May 2023
Published: 7 May 2023

Copyright: © 2023 by the authors. Licensee MDPI, Basel, Switzerland. This article is an open access article distributed under the terms and conditions of the Creative Commons Attribution (CC BY) license (https://creativecommons.org/licenses/by/4.0/).

1. Introduction

Authigenic iron-bearing minerals, developed within the upper few cm of the sediment layer, are abundant in marine sedimentary deposits ranging in age from Precambrian to recent [1–12]. The iron-bearing minerals, being sensitive to the availability of oxygen and free sulfur and Eh and pH condition, can form four different mineral species, viz. oxide, silicate, carbonate, and sulfide [13,14]. Phanerozoic iron-bearing sediments exhibit a wide range of chemical compositions, dominated by iron silicate species, including glauconite, chamosite, celadonite, and berthierine [1,6–8,15–18]. Glauconite-bearing sediments are mostly accumulated in marine sedimentary rocks ranging in depth from 30 m to 2000 m. The chemical composition of glauconites represents a broad spectrum ranging from glauconitic smectite, ferric illite, and glauconitic mica as an end-member [1,12,13]. Highly evolved glauconite, occurring in profusion, demarcates stratigraphic condensed

sections [2,6,19–21]. Although Holocene glauconites tend to form on the outer shelf and continental slope environments, ancient glauconite and other iron-bearing silicates, including chamosite and/or berthierine, occur within shallow marine transgressive sedimentary packages, especially during the Cretaceous–Paleogene time [3,4,7,8,12,22]. The widespread shallow marine iron silicates formed during the Cretaceous–Paleogene period have paleoclimatic implications. Recent studies show a close association between glauconitic sediments and warm climatic intervals [6,7,23]. The chemical reactions involving iron silicate formation, collectively known as green clay authigenesis, have been identified as a long-term climatic stabilizer for the ice-free Precambrian climate via the expulsion of CO_2 into the ocean atmospheric systems; however, such studies are limited for Phanerozoic iron silicates [24,25]. Thus, detailed knowledge of the stratigraphical and environmental implications and temporal variation of iron-rich green clays are crucial for the paleoclimatic reconstruction and evolution of seawater composition and life forms [23,26].

Paleogene sediments have attained significant attention in recent times owing to the warm climatic intervals called 'hyperthermal' events [27–29], as well as the widespread formation of iron-bearing sediments, including glauconitic shales and/or oolitic ironstones [7,20,30,31]. Although the Paleogene of India has become an important region for its economically viable lignite and hydrocarbon deposits and their rich fossil assemblages, the high abundance of authigenic glauconite within the Paleogene is often overlooked. High-resolution biostratigraphic studies and radiogenic and stable isotope stratigraphy (^{13}C, $^{87}Sr/^{86}Sr$, and $^{40}Ar/^{39}Ar$, respectively) of the Paleogene deposits in India allow the precise correlation of sedimentary sections with global events such as the Paleogene hyperthermal events [20,29,32–36]. Recent investigations have revealed the association of glauconite with major transgressions [20,23,36]. The Cambay Basin, lying south of the Kutch basin, hosts lignite-bearing sequences of the early Eocene time. The lignite and carbonaceous shale of the Cambay Shale Formation have been repeatedly interrupted by alternating limestone–green/grey shale succession comprising abundant marine fossil assemblages. Although glauconites have been reported from the Paleogene sediments of the Cambay Basin, detailed textural, chemical, and mineralogical characteristics of the iron-bearing minerals are lacking. The objectives of this paper are to (a) understand the occurrence of authigenic iron-bearing phases and highlight their genetic relationship, (b) understand the factors influencing widespread iron mineralization, and (c) understand the stratigraphic implications of abundant iron-rich phases from the Cambay Shale Formation.

2. Geological Background

The petroliferous Cambay Basin is an NNW–SSE-trending intracratonic rift basin situated on the western continental passive margin shelf of the Indian plate (Figure 1A), covering an area of approximately 53,500 km^2 [37]. This elongated basin, narrowing towards the north and opening into the Arabian Sea to the south, contains several subbasins (or blocks) separated by fault systems aligned transverse to the general trend. The detailed geology and tectonic settings of different blocks have been extensively studied and discussed [38,39]. The Cambay Basin has accumulated a 7–8 km-thick sedimentary sequence ranging in age from Cretaceous to Miocene, resting unconformably over the Precambrian basement [40,41]. Three major episodes of rifting and basin evolution are characteristic of the Cambay Basin, viz. (i) late Cretaceous to early Eocene rifting, associated with Deccan volcanics emplacement followed by tectonic subsidence, (ii) Eocene to Miocene post-rift thermal subsidence, and (iii) Miocene to present-day late post-rift structural inversion of the basin, related to the India–Asia collision [42]. Cenozoic sedimentation within the basin initiates with the deposition of ill-sorted, trap-derived volcanoclastic sediments of the Olpad (or Vagadkhol) Formation of the Paleocene age [41]. Thermal subsidence during the post-rift stage resulted in the accumulation of black shales and coarser clastic sediments of the Cambay Shale Formation. During this stage, carbonaceous shale, grey shale, and carbonates were deposited across the basin. The Miocene–Holocene late post-rift stage represents coarser clastic sediment accumulation in distinct fluvial

systems of the Babaguru, Kand, and Jhagaria formations [43]. The basin fill sediments are covered with a thick pile of Quaternary sediments.

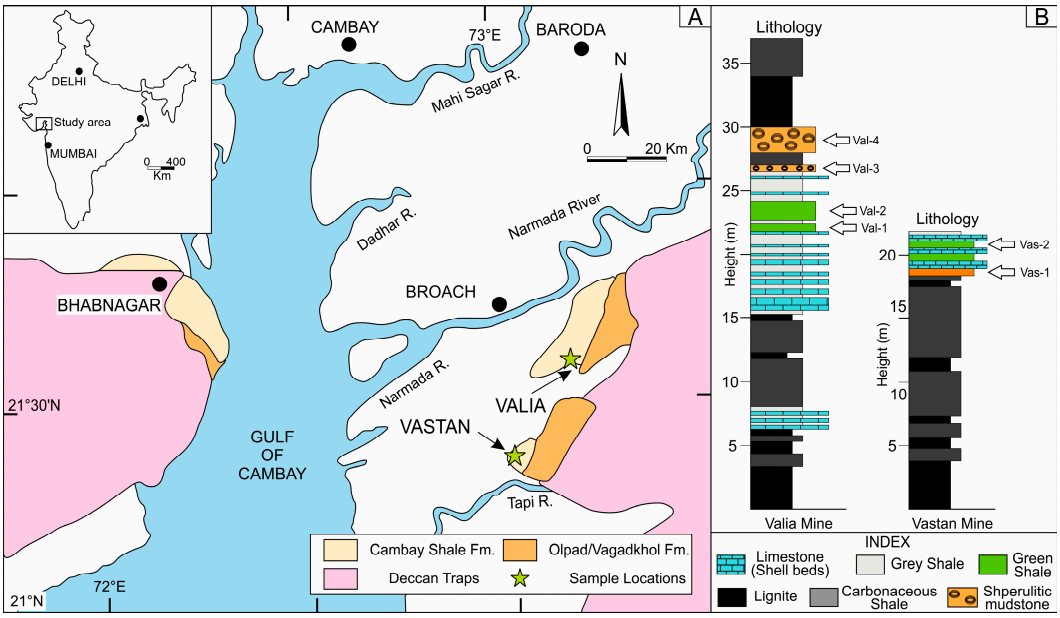

Figure 1. (**A**) Geological map of the Cambay Basin showing the extent of the Paleogene successions (modified after [33]). The locations of the studied lignite mines are marked by green stars; (**B**) Litholog of the Cambay Shale Formation at the Valia and Vastan mine sections. Note the position of the samples used for analysis marked using arrows and sample numbers.

The age of the Cambay Shale Formation has been well-established by a diverse fossil assemblage. Based on the dinoflagellate assemblage of the Cambay Shale Formation in the Vastan mine, an early Ypresian age corresponding to upper SBZ 7 to lower SBZ 10 has been designated [39]. The marine sedimentary sequence, represented by shelly limestone–green shale alternation, yielded the age-diagnostic foraminiferal assemblage of *Nummulites burdigalensis burdigalensis* and *N. burdigalensis kuepperi*, designating an SBZ 10 age for the marine incursion in the Cambay Basin [44] (see Figure 5 of [24]). The biostratigraphic age was further corroborated by the $^{40}Ar/^{39}Ar$ age of the glauconite grains from the green shale unit of the Valia mine section [33].

3. Sedimentological Background

In the Valia mine, lignite–carbonaceous shale alternation dominates the lower and upper parts of the succession. The thickness of lignite seams ranges from a few cm to 5 m, while the carbonaceous shales range in thickness from a few cm to up to 3 m (Figure 2A). In the middle part of the section, cm- to m-scale, thin limestone beds alternate with green shale. The limestone beds contain marine bivalves and larger benthic foraminifera. The green shale beds are finely laminated and contain abundant siltstone intercalations (Figure 2B). The shales exhibit green pellets arranged mostly parallel to the primary lamination, imparting a green hue for these facies. Although the green shales are mostly devoid of bioturbation, occasionally they show vertical burrows (Figure 2C). The limestone–green shale alternation is overlain by a roughly 3 m-thick spherulitic mudstone unit (Figure 2D). This unit is characterized by the presence of medium to coarse sand-sized brown spherulites randomly dispersed in a fine-grained clayey matrix. Lignite and carbonaceous shale alternations dominate the lower and upper parts of the sedimentary succession in the Vastan mine, while limestone–green shale alternations continue within the middle part of the succession. The green shales are finely laminated with minor siltstone intercalations. The shales appear brownish at the lower part due to the abundance of light-brown to dark-brown silty pellets and contain very fine lignite–carbonaceous shale

intercalations. These cm-thick limestone beds are highly fossiliferous and yield abundant foraminifera and marine bivalves. The green shales are finely laminated and contain minor siltstone intercalations.

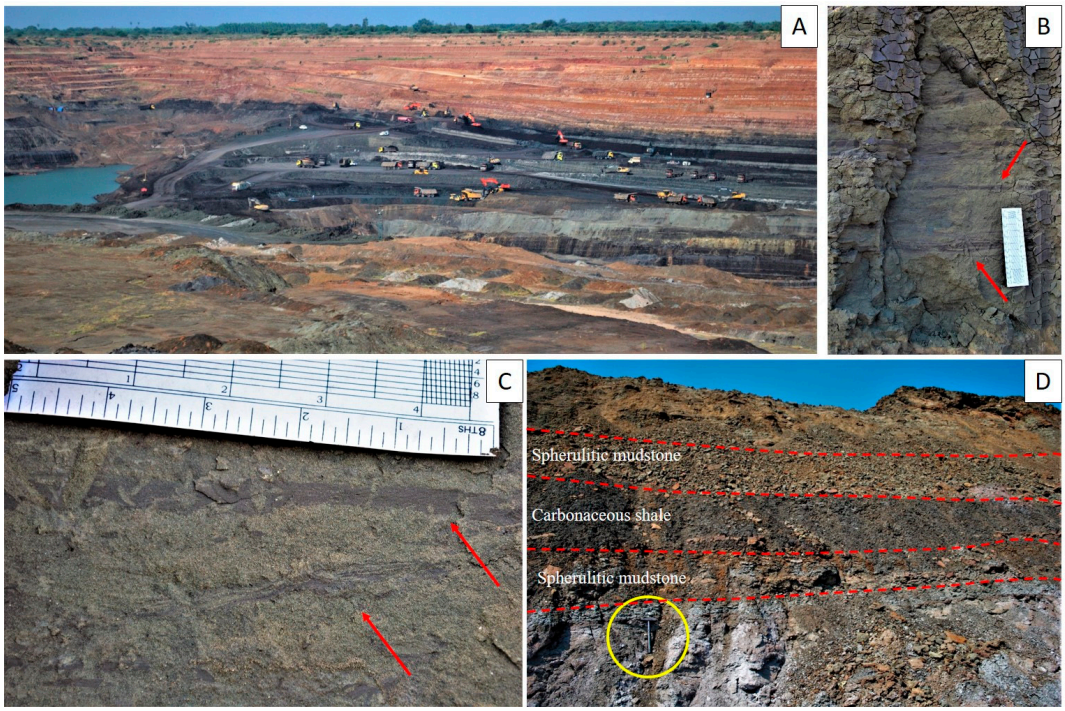

Figure 2. Field photographs showing: (**A**) the exposure of lignite-bearing sediments of the Cambay Shale Formation at the Valia lignite mine; (**B**) the vertical section of the green shale unit with thin siltstone alternations (marked with red arrow) exhibiting abundant silt-sized green pellets imparting a green hue; (**C**) close-up photograph of the green shale facies showing the alternation between the green shale and grey siltstones (marked with red arrow); (**D**) vertical section of the spherulitic mudstone facies overlying the limestone–green shale alternation; note the presence of a carbonaceous shale unit separating two horizons of the spherulitic mudstone facies (please note the hammer length for scale = 0.38 m marked with yellow circle) (the beds are marked using red dashed lines).

The dominant lignite–carbonaceous succession of the Cambay Shale Formation contains abundant leaf imprints, spores, and pollen and suggests a coastal marsh depositional environment [45]. The shelly limestone contains abundant marine fossils, representing episodes of marine flooding events [33,45–47].

4. Materials and Methods

The current study was carried out on the glauconitic green-shale-bearing Cambay Shale Formation, encountered at two different lignite mines, i.e., Valia (21°30′59.3″ N, 73°12′03.6″ E) and Vastan (21°24′31.2″ N, 73°05′39.2″ E), operated by Gujarat Industrial Power Corporation Limited (GIPCL) (Figure 1A). The open-cast lignite mines at Valia and Vastan have exposed a 100–200 m-thick, muddy succession unconformably overlying the Deccan basalts. The bottom part of the succession (unit A of [39]) crops out in the Valia mine and consists of a ~40 m-thick succession of lignite, carbonaceous shale, and grey shale alternation with intermittent shelly limestone and green shale intercalation. Representative samples for the green shales (Val-1 and Val-2) and the spherulitic mudstones (Val-3 and Val-4) were collected from the Valia mine (Figure 1B). In the Vastan mine, sampling was carried out within a ~5 m-thick shelly limestone and green/brown shale intercalation representing upper marine inundation (Vas-1 and Vas-2) (Figure 1B). Detailed logs were made for the Cambay Shale Formation from the Valia and Vastan mines, and the representative samples of the green and brown pellets and spherulites from the green shales and overlying

mudstone were collected, and their positions were marked within the litholog (Figure 1B). For the petrographic studies, two thin sections of the green shale from the Valia and Vastan mines and two thin sections of the spherulitic mudstone from the Valia mine were prepared by epoxy-curing the fissile samples. The green shales in the Valia and Vastan mines and the spherulitic mudstone overlying the green shale in the Valia mine were disintegrated and heated with Na_2CO_3 solution, followed by sieving using a 230 A.S.T.M. sieve. The coarse fractions were oven-dried, and dark-green and brown pellets and spherulites were separated from the fraction using a Zeiss Stemi 2000 stereo-zoom microscope. For X-ray diffraction analysis, 50–60 mg samples of the separated dark-green and brown pellets were gently ground into a fine powder using an agate mortar and pestle. Oriented, smear-mounted samples of the dark-green and brown pellets were prepared by preparing a slurry and pipetting it on the glass slide. The X-ray diffraction pattern of oriented aggregates of the <2 μm fraction was recorded using an Empyrean X-Ray Diffractometer with Pixel 3D detector (Cu Kα radiation, 45 kV, 40 mA) at IIT Bombay. The oriented samples were scanned from 4° to 70° with a step size of 0.026° 2θ and a scan speed of 96 s/step, under air-dried, glycolated, and heated conditions (400 °C–500 °C for 1 h). Brown spherulites of the Valia mine were analyzed from ~1 g of random powder mount (finer than 75 microns) under a similar instrumental setting. A major oxide analysis of the light-and dark-green pellets, brown pellets, and spherulites of Valia and Vastan mines was carried out on thin sections using a Cameca SX 5 Electron Probe Micro Analyzer at the Department of Earth Sciences, IIT Bombay, with an accelerating voltage of 15 kV, a specimen current of 40 nA, and a beam diameter of 1 μm (peak: 10–20s and background counting: 5–10s). Two samples from the green shale of the Valia mine and two samples from the green shale of the Vastan mine were analyzed for the major oxide analysis of green and brown pellets, while the brown spherulites were analyzed from two thin sections from the Valia mine. Natural minerals, including albite (for Na Kα), orthoclase (for K Kα), diopside (for Ca Kα, Mg Kα), apatite (for P Kα), and rhodonite (for Mn Kα), as well as synthetic mineral phases including $CaSiO_3$ (for Si Kα), Fe_2O_3 (for Fe Kα) and Al_2O_3 (for Al Kα) were used as standards for the calibration of the major oxide analysis. A duplicate analysis of the individual points showed an analytical error of less than 1%. A high-resolution micro-textural study of the hand-picked green pellet was carried out using a JSM-7600F Field Emission Gun-Scanning Electron Microscope (FEG-SEM; JEOL Ltd., Tokyo, Japan) under an accelerating voltage of 10 kV at Sophisticated Analytical Instrument Facility, IIT Bombay. An individual glauconite pellet was mounted on stubs using carbon tapes and platinum-coated to a 200 Å thickness by a sputter coater.

5. Results

5.1. Petrographic and Micro-Textural Studies of the Green and Brown Pellets and the Spherulites

In the Valia mine section, the lower part of the green shale unit is dominated by light-green pellets and angular to sub-rounded quartz grains set in a clayey matrix with sporadic appearance of dark-green pellets. The upper part of the green shale unit exhibits light-green and dark-green pellets with minor silt-sized quartz grains randomly dispersed in a clayey matrix with abundant sideritic rhomb (Figure 3A). The size and concentration of the dark-green pellets are high in the upper green shale unit compared to the lower green shale (Figure 3B). Although the green pellets are mostly rounded to sub-rounded, a few of them are elongated. The green pellets constitute ~30% to 60% of the rock by volume in some shale beds. The size of the pellet ranges from ~60 μm to ~800 μm, along the maximum elongation, and often contains inclusions of fine quartz or dolomite crystals (Figure 3B). A few pellets show penetrating deep cracks tapering inward (Figure 3B).

In the Vastan mine section, brown pellets are recorded in the lower part of the green shale unit, while the upper part is dominated by dark-green pellets and bioclast infillings (Figure 3C–E). The green shale unit of the Vastan mine section exhibits rounded to sub-rounded pellets, randomly distributed in a clayey matrix (Figure 3C). In the lower part, the pellets appear brown in plane-polarized light, imparting the brown color of the rock

and exhibiting variegated interference color under cross-polarized light. These brown pellets often contain impurities such as fine quartz particles (Figure 3D). The overlying green shale unit of the Vastan mine contains dark-green pellets with abundant foraminifera tests, randomly dispersed in a brown clayey matrix (Figure 3E). The dark-green pellets are rounded to sub-rounded, exhibiting variegated interference color under cross-polarized light. The infillings within foraminiferal chambers are brown to light-green and show a similar interference color to that of the dark-green pellets (Figure 3E).

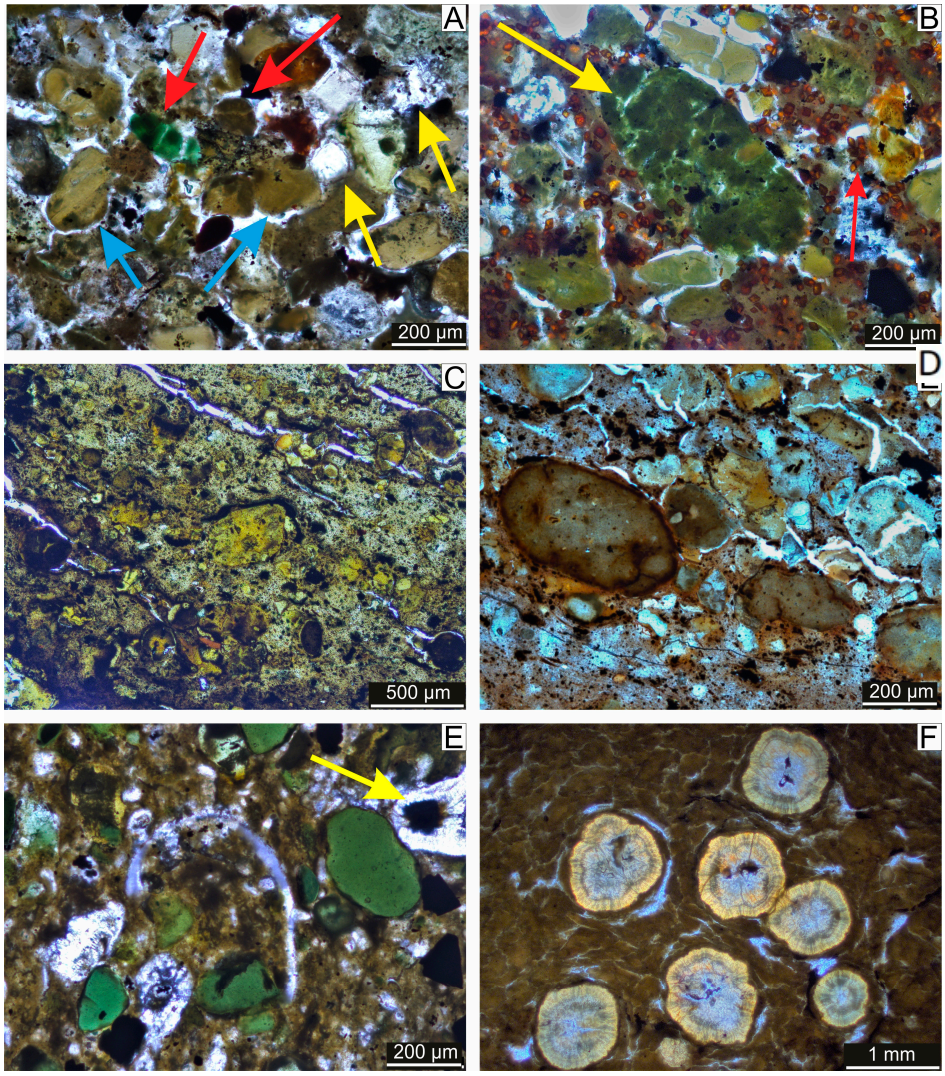

Figure 3. Photomicrograph showing: (**A**) light- and dark-green pellets (blue and red arrows, respectively) randomly dispersed in the clayey matrix of green shale facies, Valia mine. Note the presence of both angular and rounded quartz grains in the matrix (marked with yellow arrow); (**B**) elongated pellets with inward tapering cracks (marked with yellow arrow) in green shale facies, Valia mine. Note the presence of sideritic rhombs (red arrow) randomly dispersed in the matrix; (**C**) variegated interference color of pellets (marked by yellow arrow) randomly distributed in a clayey matrix of the green shale, Vastan mine; (**D**) rounded to sub-rounded brown pellets with fine quartz impurities in the green shale, Vastan mine (yellow arrow); (**E**) abundant light- to dark-green pellets with dark-brown secondary mineral formation within foraminiferal chambers (marked with yellow arrow) of the green shale unit, Vastan mine; (**F**) spherulitic mudstone facies showing rounded to sub-rounded spherulites with radially arranged siderite crystals forming the prominent rim of the spherulites.

The spherulitic mudstone unit of the Valia mine section is represented by rounded to sub-rounded brown spherulites randomly dispersed in a clayey matrix. The clayey matrix is highly bioturbated, destroying primary sedimentary laminae (Figure 3F). The spherulites appear yellow to yellowish brown under plane-polarized light and exhibit variegated interference color under cross-polarized light imparted by the finely arranged crystals on the rim of the spherulites. The diameter of the spherulites ranges from ~90 µm to up to 2 mm. The core of the spherulites is finely crystalline, while the rim of the spherulites is formed from a radial arrangement of fine crystal aggregates (Figure 3F). In general, the majority of the spherulites are distinctly separate and only constitute ~30% of the total rock by volume. However, in some places, spherulite concentration often exceeds 50% of the total rock volume, and the spherulites exhibit a sutured grain boundary (Figure 3F). The clayey matrix is compacted around large siderite spherules (Figure 3F).

Under the high-resolution scanning electron microscope, the dark-green pellet with faintly developed cracks (Figure 4A) reveals tiny, curved, blade-like structures arranged in a rose petal structure (Figure 4B–D). These blades are very thin, <1 µm in thickness, and vary from 1–3 µm in length. The rosette structures, typical of evolved glauconite, are often clustered in some places, surrounded by ill-developed, curly blade-like protrusions resembling slightly evolved glauconite (Figure 4C,D) [1,20,36]. In a rare instance, the rosette structure of the glauconite is formed on some plate-like structures of probable kaolinite (Figure 3C).

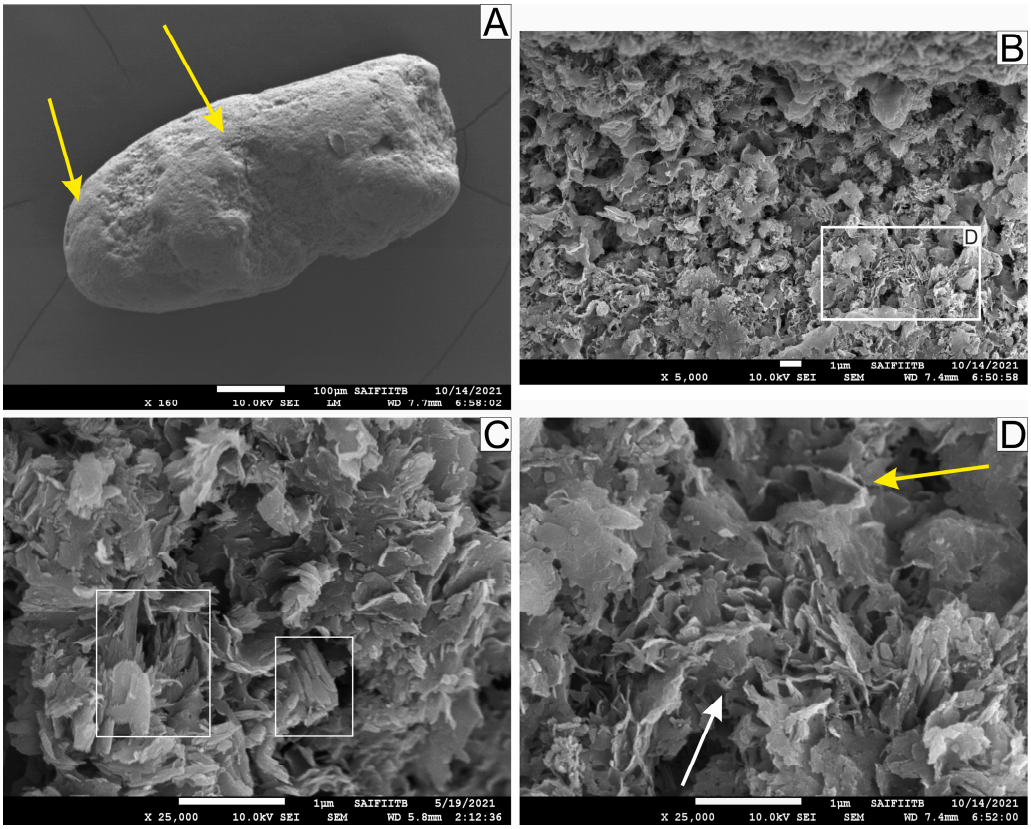

Figure 4. High-resolution scanning electron microscope showing elongated, glauconite pellet with faintly developed cracks (yellow arrows) (**A**) with small clusters of 'rosette' arrangements of glauconite blades (**B**). Development of glauconite rosette structure on some plate-like clay substrates (white box) (**C**) and the enlarged image of the glauconite rosette structure (white arrow) exhibiting ill-developed, curly blades of slightly evolved glauconite (yellow arrow) (**D**).

5.2. Mineralogy of the Green and Brown Pellets and the Spherulites

The X-ray diffraction pattern of the hand-picked, separated dark-green pellets of the Vastan mine section exhibits asymmetric and broad-based reflections at 10.41 Å, 4.51 Å, 3.34 Å, 1.98 Å, and 1.52 Å (Figure 5) under air-dried conditions. Several small but sharp peaks also appear at 4.25 Å, 2.59 Å, 2.45 Å, 2.28 Å, 2.24 Å, 2.13 Å, 1.82 Å, and 1.54 Å (Figure 5). On treatment with ethylene glycol, the 10.41 Å expands and forms a doublet at 9.93 Å and 10.87 Å (Figure 5). This peak collapses to 10.16 Å after heating at 550 °C for 1 h (Figure 5). Other prominent reflections show little or no shift upon glycolation and heating treatment. The air-dried sample of hand-picked, separated brown pellets, however, exhibits mostly asymmetric and broad-based basal reflections when analyzed in oriented, smear-mounted samples. The peaks are situated at 14.72 Å, 7.31 Å, 4.58 Å, 3.60 Å, 3.12 Å, 2.80 Å, 2.71 Å, 1.63 Å, 1.56 Å and 1.52 Å (Figure 6). Upon glycolation, these reflections rarely shift positions (Figure 6). Although after heating at 550 °C for 1 hour, the peak at 14.72 Å broadens significantly, and the intensity of the peak at 7.31 Å diminishes drastically; the remaining peaks record little or no significant shifts (Figure 6). The brown spherulites of the Valia mine section exhibit a few sharp and symmetric peaks at 3.60 Å, 2.80 Å, 2.35 Å, 2.14 Å, 1.97 Å, and 1.73 Å with a few minor peaks at 1.80 Å, 1.51 Å, 1.43 Å, and 1.39 Å (Figure 7).

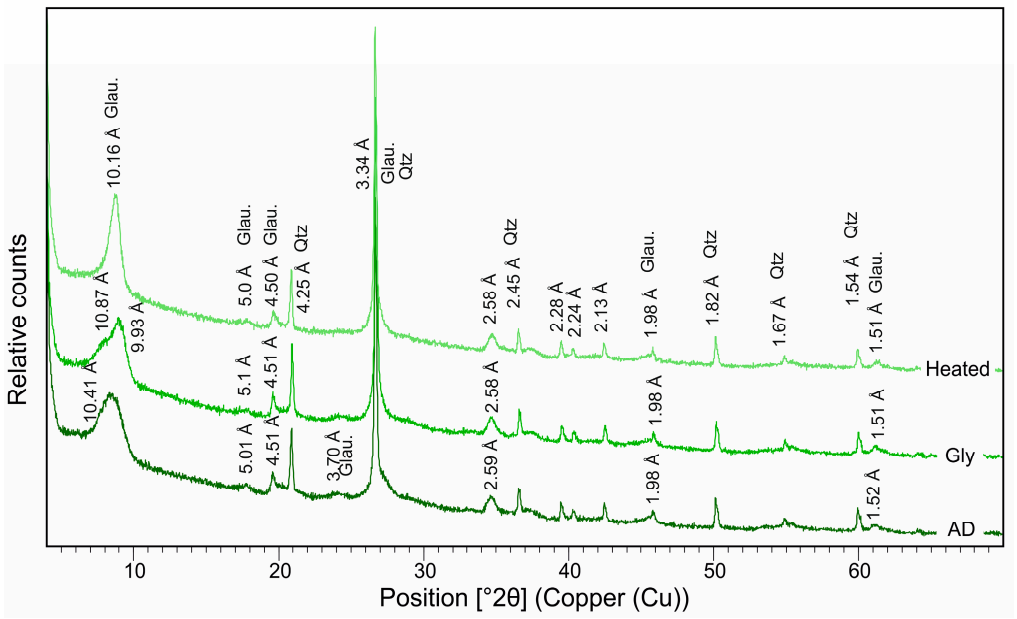

Figure 5. X-ray diffraction pattern of oriented smear mount of separated dark-green glauconite pellets in Vastan mine in air-dried (AD), glycolated (Gly), and heated (Heated) conditions (Glau. = glauconite and Qtz = quartz).

The dark-green pellets from the Vastan mine are identified as glauconites based on the broad-based peak of the (001) basal reflection at 10.41 Å, the subdued intensity of the (002) reflection at 5.01 Å, and the presence of a faint $\left(112\right)$ reflection at 3.70 Å [1,5,21,48–50]. The $d_{(001)}$ (distance between (001) and (020) peaks) value ($d_{(001)}$ = 11.17° 2θ) suggests a slightly evolved glauconitic composition, which is corroborated by the mineral chemical data (see supplementary Tables S1–S3) [2]. The subdued intensity of the (002) reflection indicates significant Fe substitution in the octahedral layers [2,49,51]. The expansion of the basal (001) reflection and the formation of two distinct peaks with variable intensity suggests significant smectite interstratification (possibly 10%–30%) of the glauconite mineral. However, the (060) reflection at 1.51 Å indicates a di-octahedral nature of the dark-green glauconite pellets. The sharp and symmetrical reflections at 4.25 Å, 3.34 Å, 1.82 Å, and 1.54 Å suggest quartz impurity.

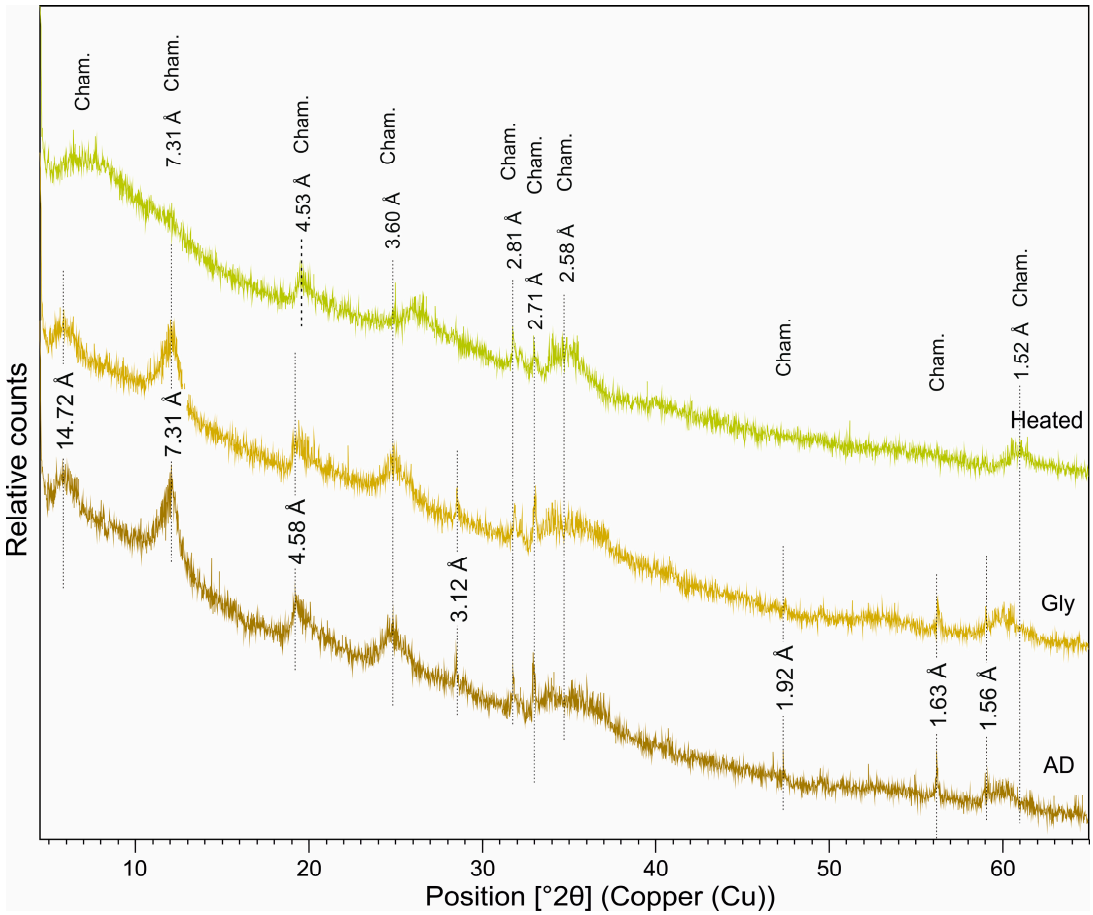

Figure 6. X-ray diffraction pattern of oriented smear mount of separated brown chamosite pellets in Vastan mine in air-dried (AD), glycolated (Gly), and heated (Heated) conditions (Cham. = chamosite).

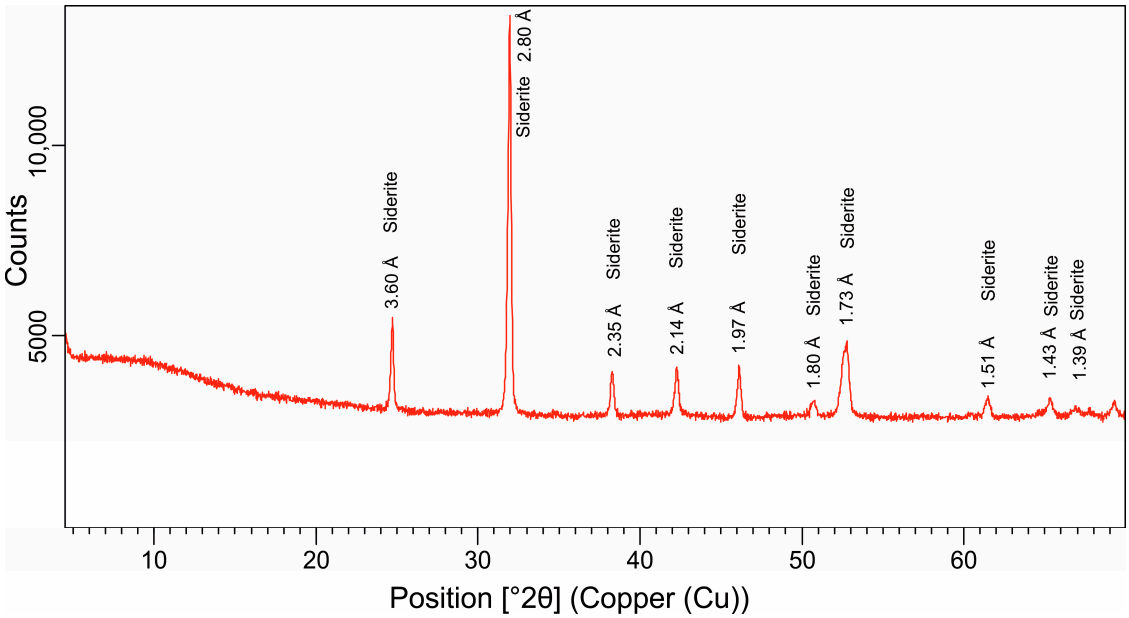

Figure 7. X-ray diffraction pattern of randomly oriented powdered sample of separated brown spherulites from the spherulitic mudstone unit of the Valia mine indicating the siderite mineralogy.

The brown pellets from the Vastan mine show a characteristic X-ray diffraction pattern of chamosite, characterized by a weak basal (001) reflection at 14.32 Å and strong basal

reflections of (002) and (004) at 7.30 Å and 3.57 Å [10]. The mineral chemical data and petrographic observation further attest to this interpretation [10,17,52]. The brown spherulites with sharp, symmetric peaks are identified as siderite from the characteristic reflections at 3.60 Å, 2.80 Å, 2.14 Å and 1.74 Å [36].

5.3. Major Element Composition of Green and Brown Pellets and the Spherulites

Dark-green and light-green pellets of the green shale units of the Valia mine section are compositionally different. The K_2O content of the dark-green pellets exhibits a wide range from 1.10 to 5.00 wt.% (av. 2.80 wt.%) (Supplementary Table S1). The Fe_2O_3(total) content of the dark-green pellets is variable, ranging from 6.70 to 22.40 wt.% (av. 14.70 wt.%) (Supplementary Table S1). The MgO content of the dark-green pellets varies between 1.90 and 4.00 wt.% (av. 3.20 wt.%), while the SiO_2 content ranges from 47.20 to 58.70 wt.% (av. 53.80 wt.%) (Supplementary Table S1). The Al_2O_3 content of the dark-green pellets remains high, ranging from 11.90 to 25.60 wt.% (average 16.40 wt.%) (Supplementary Table S1). On the other hand, the light-green pellets in the green shale unit exhibit low K_2O content (<1 wt.% K_2O). The Fe_2O_3(total) content of the light-green grains is also low, ranging from 7.30 to 16.80 wt.% (av. 9.70 wt.%) (Supplementary Table S1). The light-green grains exhibit a broad spectrum of MgO content, ranging from 1.50 to 6.10 wt.% (av. 3.00 wt.%), while the SiO_2 content of these grains varies between 49.10 and 61.30 wt.% (av. 56.60 wt.%) (Supplementary Table S1). The Al_2O_3 content of the light-green grains remains abnormally high, ranging from 17.70 to 35.10 wt.% (av. 22.70 wt.%) (Supplementary Table S1).

The green and brown pellets and the bioclast infillings of the green shales from the Vastan mine section represent distinct compositional domains defined by K-rich green pellets and K-poor brown pellets and bioclast infillings. The green pellets from the Vastan mine exhibit a highly variable K_2O concentration ranging from 1.46 to 7.77 wt.% (av. 4.86 wt.%) (Supplementary Table S2). The Fe_2O_3(total) content of these green pellets is consistently high (av. 25.94 wt.%) (Supplementary Table S2). The Al_2O_3 content of the green pellets varies significantly, ranging from 5.94 to 15.11 wt.% (av. 9.29 wt.%). The MgO content is also high (av. 7.94 wt.%). The brown bioclast infillings within the same unit reflect a K-poor (<1.0 wt.% K_2O) and Fe-rich (av. 31. 45 wt.% Fe_2O_3(total)) composition compared to the green pellets. The Al_2O_3 content of the bioclast infillings is almost similar to the green pellets (av. 9.30 wt.% Al2O3); however, the MgO content of the bioclast infillings is unusually high, ranging from 11.79 to 14.86 wt.% (av. 13.60 wt.%) (Supplementary Table S2).

The brown pellets also show consistently low K_2O content (0.10 to 1.00 wt.% with av. 0.60 wt.%) (Supplementary Table S2). The Fe_2O_3(total) content of the brown pellets is distinctly higher than that of the green pellets, ranging from 20.50 to 49.60 wt.% (av. 38.20 wt.%) (Supplementary Table S2). The MgO content of the brown pellets is low, varying from 1.40 to 3.50 wt.% (av. 2.47 wt.%) (Supplementary Table S2). The Al_2O_3 content of the brown pellets ranges from 8.17 to 25.47 wt.% (av. 14.04 wt.%) (Supplementary Table S2). The SiO_2 content of most of the brown pellets shows <40 wt.% SiO_2 content (Supplementary Table S2).

The spherulites in the Valia mine reveal a Fe-rich composition, i.e., > 95% $FeCO_3$ with minor impurities, including $CaCO_3$ and $MgCO_3$ (Supplementary Table S3).

All data points were normalized to 100 wt.% on an anhydrous basis for the bi-variate analysis/plot (Figures 8 and 9). The light- and dark-green pellets from the Valia mines display two distinct clusters. The dark-green pellets exhibit a positive correlation for K_2O and Fe_2O_3(total) (correlation coefficient, $r = 0.80$, p(a) < 0.001, $n = 18$) (Figure 8A). The K_2O and Fe_2O_3(total) contents of the light-green pellets are lower than that of the dark-green grains and exhibit a cluster of data points with a poor correlation. The Al_2O_3 vs. Fe_2O_3(total) cross-plot of the dark-green pellets exhibits a negative correlation (correlation coefficient, $r = -0.82$, p(a) < 0.001, $n = 18$) (Figure 8B). The light-green grains are enriched in Al_2O_3 compared to the dark-green pellets.

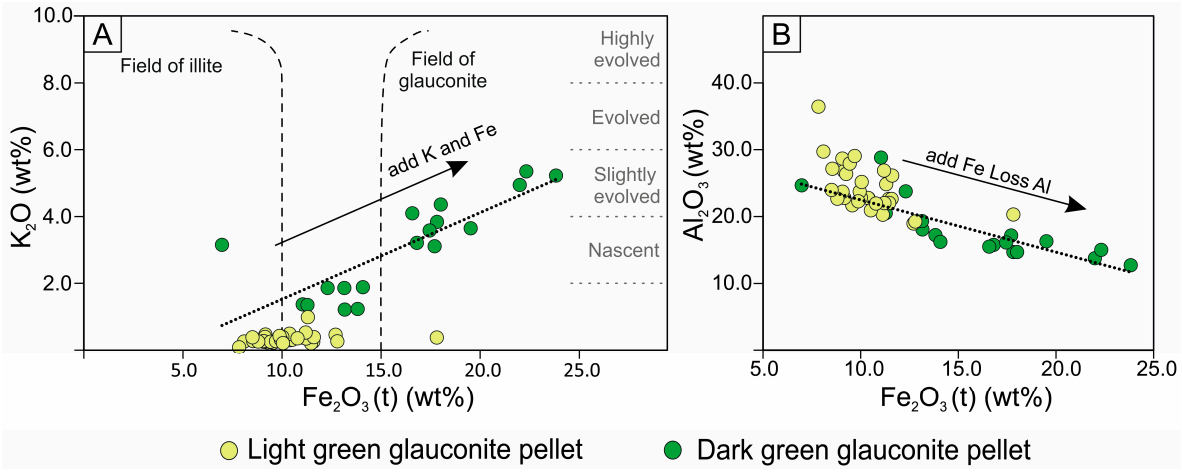

Figure 8. Cross-plots of K_2O vs. Fe_2O_3(total) (**A**) and Al_2O_3 vs. Fe_2O_3(total) (**B**) of light-green and dark-green glauconite pellets in the green shale facies of Valia mine. Note that only the dark-green pellets exhibit a moderate positive correlation in the K_2O vs. Fe_2O_3(total) cross-plot and the negative correlation of the Al_2O_3 vs. Fe_2O_3(total) cross-plot.

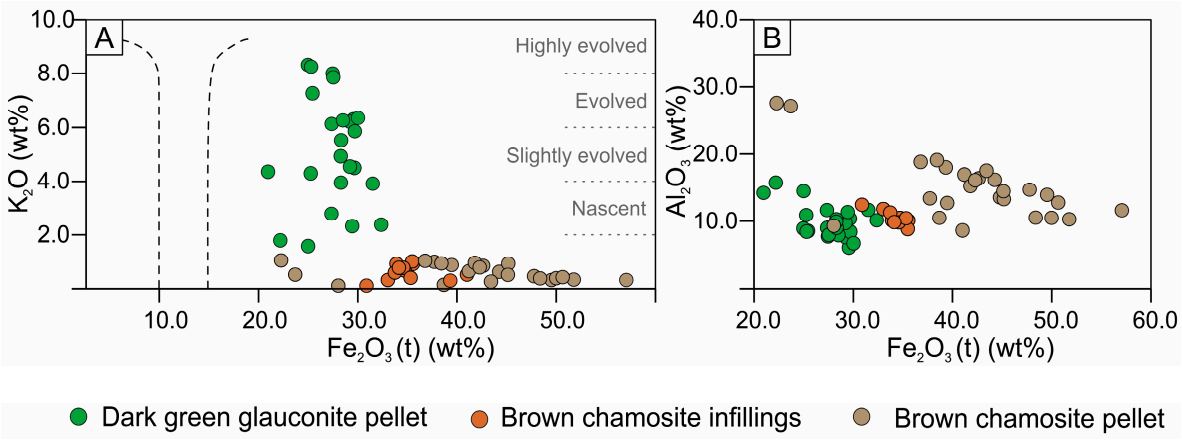

Figure 9. Cross-plots of K_2O vs. Fe_2O_3(total) (**A**) and Al_2O_3 vs. Fe_2O_3(total) (**B**) of the dark-green glauconite pellets and brown chamosite pellets in the green shale of Vastan mine. Note that the data points form two distinct clusters in K_2O vs. Fe_2O_3(total) cross-plot.

The X-ray mapping of the bioclast infilling and green pellet reveals a clear distinction between the K-rich green pellet and K-poor bioclast infillings (Figure 9A–C). The MgO content of the green pellets are variable but are consistently low compared to that of the bioclast infillings (Figure 9F). The bioclast infillings show a complete dissolution of the calcite test and replacement with chamosite clay (Figure 9A–F).

6. Discussion

6.1. Origin of the Glauconite, Chamosite, and Siderite in the Cambay Shale Formation

6.1.1. Glauconite

Three popular hypotheses explain glauconite formation at the sediment–seawater interface, viz. the 'layer lattice theory' of [53], the 'verdissement theory' of [1], and the 'pseudomorphic replacement theory' of [11]. Different hypotheses postulate different substrates for glauconite, resulting in a different chemical pathway for glauconite evolution [1,2,48,49,53–55]. Verdissement involves the initial precipitation of Fe-rich smectite and its subsequent evolution to glauconite via K_2O incorporation. Glauconite forms via the pseudomorphic replacement of other minerals (mostly feldspar) and evolves through Fe_2O_3 incorporation in high-K-activity pore water [17]. The glauconite formation from a degraded

layer lattice structure (mostly phyllosilicates) requires the simultaneous incorporation of K_2O and Fe_2O_3 into the glauconite structure [20,53].

The petrographic studies coupled with the mineralogical and mineral geochemical studies identify the light- and dark-green pellets from the Valia mine and the green pellets of the Vastan mine as glauconite. The significant difference in the grain size among the pellets and the surrounding matrix (Figure 3A–B) and the presence of radial cracks in some pellets suggest the authigenic nature of the glauconite pellets. Ideally, glauconite exhibits a wide-ranging chemical composition with variable K_2O (2–10 wt.%), Fe_2O_3(total) (20–25 wt.%), and Al_2O_3 content (3–11 wt.%) [56]. Both the light-green pellets of the Valia mine section and the dark-green pellets of both the Valia and Vastan mines plot within the permissible range of glauconitic composition (Figures 8 and 9). The chemical composition of the light-green and some dark-green grains of the Valia mine represents a glauconite–smectite composition with <15 wt.% Fe_2O_3(total) content. The good positive correlation of the K_2O vs. Fe_2O_3(total) cross-plot for the dark-green pellets suggests the addition of K_2O and Fe_2O_3(total) into the glauconite structure, referring to the 'layer lattice theory' of glauconite formation [54]. Both the light-green and dark-green pellets contain a high amount of Al_2O_3. The good negative correlation of the Al_2O_3 and Fe_2O_3(total) cross-plot for the dark-green pellets corroborates that the glauconitization reaction involves an octahedral Al-for-Fe substitution [1,6,20,21,36,55,57]. The charge imbalance arising from the substitution of trivalent Al^{3+} by bivalent Fe^{2+} is responsible for the incorporation of monovalent cations such as K^+ (and occasionally Na^+, as shown in Table S1) into the interlayer cationic sites. The SiO_2 and MgO content of the light-green and dark-green grains of the Valia mine are quite similar, resulting in poor correlation among K_2O, SiO_2, and MgO (not presented). The light-green pellets exhibit poor correlation among different cross-plots due to very low K_2O content and wide-ranging Al_2O_3 and Fe_2O_3(total) contents. On the other hand, the dark-green pellets of the Vastan mine have moderate K_2O content with high Fe_2O_3(total) and low Al_2O_3 contents. The composition of the green pellets in the Vastan mine satisfies the 'ideal' glauconite composition with >15 wt.% Fe_2O_3(total), which is further attested by the mineralogical investigations.

The characteristic rounded-to-sub-rounded pellet morphology, without any trace of the substrate mineral, suggests a fecal pellet or clay pellet substrate (Figure 3A–E). The glauconite of the Cambay Shale Formation evolved via an octahedral Al-for-Fe substitution followed by K_2O intake into its crystal structure, reflecting a moderate positive correlation in the K_2O vs. Fe_2O_3 cross-plot (Figures 8A and 9A). The chemical evolution pathway of the Cambay Shale Formation corroborates the 'layer lattice theory'. Glauconite pellets with a similar high Al_2O_3 (>10 wt.%) and relatively moderate-to-high Fe_2O_3 (>15 wt.%) content have been reported primarily from Paleogene sediments of Cenozoic time [7,23]. A few glauconites from the Mesozoic and Paleozoic times have also shown similar geochemical signatures [21,58–60]. The factors responsible for the anomalously high Al_2O_3 content of glauconites include freshwater input into the depositional environment [48], diagenetic alteration [59], and late diagenetic exhumation and chemical weathering due to groundwater [57,61–63]. Shallow marine glauconites are essentially Al-rich, and the deep-marine variety is Fe-rich [5]. The entry of Al_2O_3 in the glauconite structure is often followed by the exit of Fe_2O_3, resulting in a low content of Fe_2O_3 (<10 wt.%). Recent investigations have identified abundant glauconite pellet transformation from a kaolinite-rich substrate showing high Al_2O_3 content despite a moderate-to-high Fe_2O_3 (>15 wt.%) content. The compositional homogeneity of individual glauconite pellets and the absence of any visible alteration rim in the glauconite pellets rules out any diagenetic alteration or episodes of exhumation and chemical weathering [57,61–63]. Increased freshwater input into the depositional environment can lower the K^+ activity in the seawater, resulting in a low content of K_2O in glauconite [20,48,60]. This allows us to demarcate zones of high surface run-off within the marginal marine depositional environment [48]. The Valia mine successions, representing shallower water depth compared to the Vastan mine, produce K-poor glauconites, most likely related to increased freshwater influx

into the depositional environment. The glauconite of the Cambay Shale Formation was possibly formed by the transformation of a kaolinite-rich clayey substrate reacting with Fe–(oxy)hydroxides and minor smectite under mildly reducing conditions [20,23,64,65].

6.1.2. Chamosite

The petrographic observations, corroborated by mineralogical and mineral geochemical studies, identify two distinct modes of occurrences of chamosite, i.e., brown pellets and bioclast infillings. The brown pellets, concentrated at the lower part of the Vastan mine section, and the bioclast infillings, observed within the upper part of the same section (Figure 3C–E), exhibit a distinct chemical composition defined by K_2O-poor but Fe_2O_3(total)-rich chamosite. The K_2O vs. Fe_2O_3(total) cross-plot of the brown pellets and bioclast infillings exhibits a very poor correlation arising from the low K_2O content (Figure 9A). The Al_2O_3 vs. Fe_2O_3(total) cross-plot displays two different clusters of datapoints, with the bioclast infillings being less Al_2O_3-rich compared to the brown pellets (Figure 9B). The MgO contents of the brown pellets and bioclast infillings are significantly different. The X-ray mapping of the bioclast infillings reveals the extensive dissolution of the bioclast prior to chamosite formation (Figure 10).

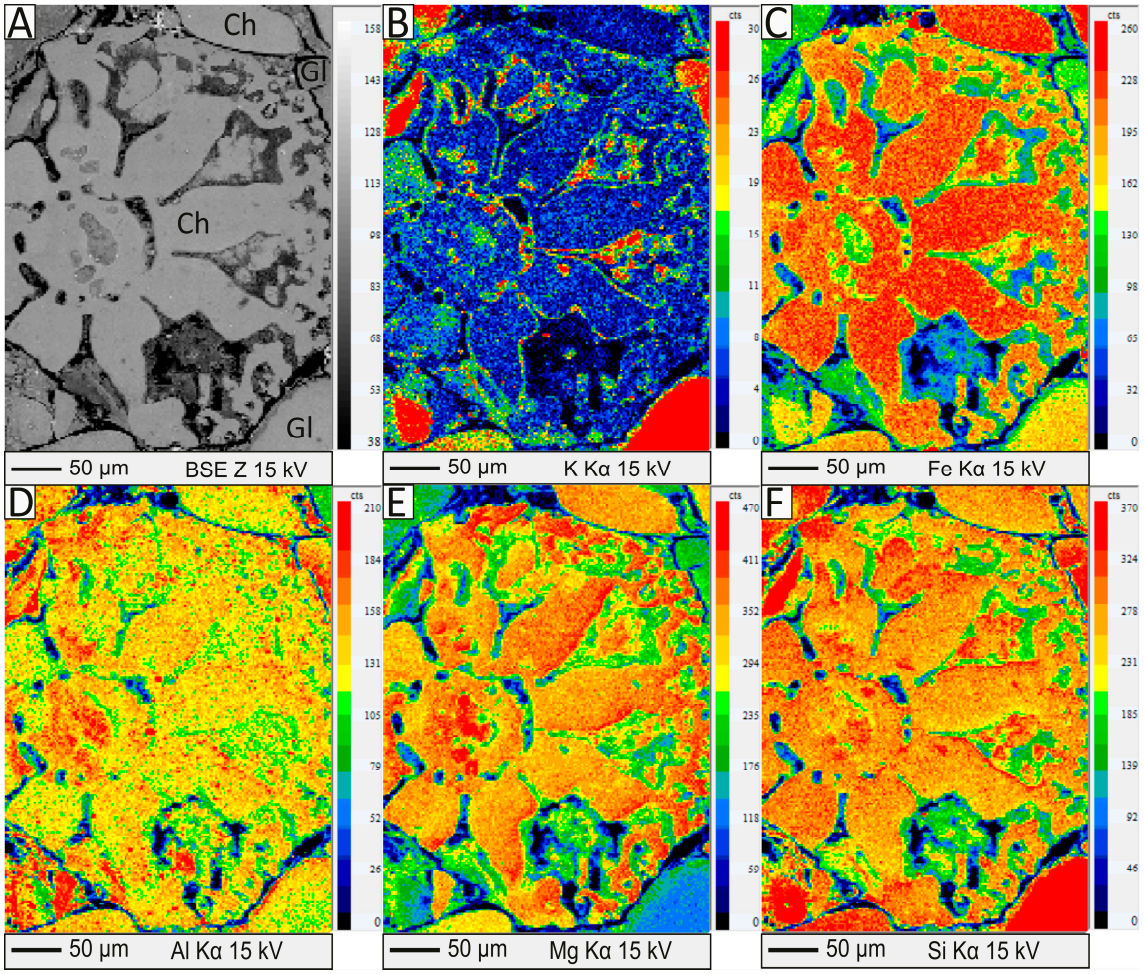

Figure 10. Back-scattered Electron (BSE) mapping (**A**) and X-ray mapping of the bioclast infillings from the green shale of the Vastan mine section showing the relative contraction of K, Fe, Al, Mg, and Si measured using EPMA (**B**–**F**). Note the compositional differences between green glauconite pellet (Gl) and bioclast infillings of chamosite (Ch).

Chamosite, a trioctahedral Fe-rich chlorite, generally forms through the transformation of berthierine at elevated temperatures of >70 °C during late diagenesis [10,15,17]. The

dominance of lignite within the Vastan mine rules out the influence of high temperature. The formation of iron-bearing authigenic mineral phases is regulated by the depositional redox condition and the iron reduction reaction [7,26]. Chamosite pellets may form by the reaction of kaolinite and Fe–(oxy)hydroxide with an abundant supply of organic matter and a detrital input of iron. A slightly alkaline pH in an anoxic (non-sulfidic) depositional environment favors chamosite formation [66]. The confined chambers of dead organisms (mostly benthic foraminifera) provide the ideal microenvironment for chamosite formation. The solubility of iron in the Fe^{2+} state increases in anoxic conditions, which quickly becomes fixed into a silicate (or carbonate) structure. In the Precambrian shallow marine sediments from China, chamosite pellets originated from the alteration of existing glauconite pellets under ferruginous seawater conditions [10]. The co-occurrence of chamosite and glauconite in the Cambay Shale Formation suggests a shift in depositional redox condition, probably facilitated by the enhanced decomposition of organic content. The presence of thin bands of lignite alternating with carbonaceous shales corroborates the strongly reducing condition, favoring chamosite formation rather than glauconite.

6.1.3. Siderite

Siderite is an iron carbonate formed as cement or distinct nodules/ooids in either freshwater or marine depositional environments [67]. Siderites of the Cambay Shale Formation appear as fine to coarse sand-sized, light-brown to dark-brown spherulites within the spherulitic mudstone unit overlying the limestone–green shale alternation in the Valia lignite mine. Morphologically, the siderite spherules closely resemble the 'perfect spherules' (sphaerosiderite) [68], although the core and the rim in our sample show a distinct optical discontinuity. The spherules form concentric crystals on a cryptocrystalline core. The geochemical environment for siderite formation is quite restricted compared to the formation of iron silicates such as glauconite and chamosite. Although the mobility of iron is permitted in the anoxic condition in the Fe^{2+} state, the presence of sulfide in the depositional environments, even in small quantities, inhibits siderite formation and favors pyrite formation [14,67,69]. The geochemical composition of these siderites represents pure carbonate composition, rich in iron (>95 wt.%) with minor impurities (<5 wt.%), suggesting its formation under the influence of freshwater conditions [67,69]. Freshwater siderites are primarily associated with strongly reducing (methanogenic zone) conditions, in which a high concentration of organic matter and a high sedimentation rate provide a reducing condition without a significant input of sulfur. The occurrences of sideritic spherulite within the Cambay Shale Basin mark regressive deposits.

6.2. Stratigraphic Implication of Authigenic Green Clays in Cambay Shale Formation

Recent studies have demonstrated that the formation of authigenic green clay minerals, such as glauconite, chamosite, and other Fe-bearing minerals, including oolitic ironstones, are favored during the warm climatic intervals of the Mesozoic and Cenozoic [6–9]. Authigenic green clay formation is particularly abundant in sedimentary deposits associated with warm climatic intervals, known as hyperthermal events [7,23]. The early Eocene sediments of the Cambay Shale Formation have attained significant attention owing to the discovery of multiple hyperthermal events [29,33,47]. Paleocene Eocene Thermal Maximum (PETM) and Eocene Thermal Maximum-2 (ETM-2) are reported from the outcrop section at the Vastan mine and the borehole section of the Cambay Shale Formation from the Valia mine, respectively [33]. They provided the $^{40}Ar/^{39}Ar$ age of the glauconite from lower green shales from the Vastan mine (56.6 ± 0.7 Ma) and Valia mine (52.6 ± 1.0 Ma). Recently some workers explained the origin of glauconite in the same section in relation to hyperthermal events [23]. These authors also demonstrated the genetic linkage between glauconitization and hyperthermal events in the adjacent Barmer, Jaisalmer, and Kutch Basins [23]. The glauconitic green shales, alternating with fossiliferous limestone and grey shale, demarcates the major flooding surfaces in these basins.

The Cambay Shale Formation, spanning from the late Paleocene to the early Eocene, has two glauconitic horizons. The older ones, recovered from a borehole from the Valia mine, are dated using the $^{40}Ar/^{39}Ar$ method. The age of this glauconite coincides with the onset of the PETM [33]. The younger glauconite in the same mine coincides with the ETM-2 hyperthermal event [33]. Glauconite-pellet-bearing green shale facies of the Valia mine section, overlying the fossiliferous limestone beds containing *Nummulites burdigalensis burdigalensis,* represent a marine incursion event. The presence of *N. burdigalensis burdigalensis* demarcates the age of the marine incursion as SBZ 10 [44,70]. The marine incursion resulted in a drastic change in the sedimentary pattern as the marginal marine lignite–carbonaceous shale alternation was replaced by a limestone–green shale alternation, containing abundant glauconite pellets. Similar to the Cambay Shale Formation, the record of hyperthermal events is often demarcated by a dramatic shift from glauconite-rich green shale to kaolinite-rich grey shale across the PETM [7,20,31,71,72]. These episodes of warm climatic intervals are characterized by the strong hydrolysis of the continent, intense chemical weathering, increased precipitation, high surface run-off, and a subsequent increase in kaolinite and amorphous Fe^{3+} (as iron–(oxy)hydroxides) influx into the shallow marine environment [20,31,72–75], facilitating a suitable depositional environment for widespread authigenic glauconite formations. Therefore, the mineralogical transition across the hyperthermal events requires further investigations to constrain the roles of warm climatic intervals and sedimentation patterns on bio-limiting elements such as iron. The Cambay Shale Formation, hosting an array of iron-bearing minerals including glauconitic smectite to glauconite, chamosite, and siderite, has the potential to elucidate the fate of iron in the shallow marine depositional environment.

6.3. Implications of Authigenic Fe Mineralization in Shallow to Marginal Marine Sediments

Sideritic mudstone, although occurring in small numbers throughout the geologic past, constitutes a significant component of the oolitic ironstone facies containing > 5% oolith/ooid/peloid as a framework constituent and is composed of >15 wt.% iron with goethite (iron oxide), siderite (iron carbonate), berthierine and chamosite (iron silicate) [7–9,15,18,76,77]. The proliferation of oolitic ironstone throughout the geologic past was not uniform. It peaked during the Ordovician to Devonian and Jurassic to middle Cenozoic periods [8]. Most of the Paleogene oolitic ironstone deposits are associated with glauconite, phosphorite, hardground, or coal measures, indicating a close relationship among them. Many sedimentary basins host oolitic ironstone and glauconite associations in late Paleocene–early Eocene, middle Eocene, and late Oligocene intervals corresponding to warm climatic intervals [7,68]. Although abundantly found around the world, Paleogene oolitic ironstone and glauconite associations are rare in the Indian subcontinent. The only exception may be the Subathu Formation, which has recorded possible oolitic ironstone beds with glauconitic shales [78]. The presence of early Eocene siderite-bearing spherulitic mudstone deposits in the Cambay Shale Formation has paleoclimatic implications.

The dominant mechanism of oolitic ironstone formation shifted throughout the geologic past. However, the Paleozoic oolitic ironstones, primarily formed in shallow epicontinental seas and associated with phosphorite deposits, demarcate origin through the upwelling of ferruginous bottom water with minor volcanogenic Fe input [77]. Cenozoic oolitic ironstones may form by hydrothermal methane venting [18]. Although occurring in small numbers, nodular sideritic and/or pyritic mudstones are reported from littoral facies, often expressed within cyclic deposits of shales, coal/lignite, and oolitic ironstone [8,79]. The sedimentological and geochemical signature of the siderite-bearing spherulitic mudstone in the Valia mine indicates a nonmarine, freshwater depositional condition with negligible marine influence. The sideritic mudstones overlying the marine interval possibly represent the initiation of early Eocene marine regression in the western Indian continental margin [45]. Siderite spherulites can abundantly form in organic-rich, reducing freshwater systems, including lakes, swamps, and marshes [80,81]. The warm and humid climate of the early Eocene enhanced hydrological cycle, coupled with an increased rate of chemical

weathering, has supplied abundant Fe–(oxy)hydroxides in the depositional environment, whereas the development of thick mangrove vegetation provided sufficient organic matter. The reducing and freshwater conditions facilitate the formation of siderite [82]. The decomposition of organic matter and the absence of free sulfide in the depositional environment provided the necessary anoxic condition for Fe–carbonate formation and inhibited iron sulfide (pyrite) formations [7,18].

7. Conclusions

The conclusions of the present study include the following:

(A) The lignite-bearing marginal marine Cambay Shale Formation hosts episodes of marine incursions, which are reflected in the accumulation of limestone–green shale alternations in the Valia and Vastan mines.

(B) The marine incursions are characterized by authigenic Fe–silicates such as glauconite and chamosite. The overlying regressive deposits exhibit abundant authigenic Fe mineralization in the form of siderite spherulites.

(C) The moderate K_2O content and characteristic basal (00*l*) reflections indicate the 'slightly evolved' nature of glauconite in the dark-green pellets in the Cambay Shale Formation. These glauconites are rich in Al_2O_3 with a moderate-to-high Fe_2O_3(total) content. The brown pellets with a low SiO_2 and negligible K_2O content have a (001) reflection at 14.32 Å, which demarcates a chamositic composition. The brown spherulites, on the other hand, are almost entirely composed of $FeCO_3$, exhibit a monomineralic siderite composition, and represent freshwater influence.

(D) The green glauconite pellets of the Valia mine are less matured and contain less K_2O, Fe_2O_3(total), and more Al_2O_3 compared to the Vastan mine. On the contrary, the Vastan mine contains significant chamosite pellets, suggesting a more anoxic depositional condition at the lower part of the succession. Freshwater influx is the prime reason for the poor maturation of glauconites in the Valia mine.

Supplementary Materials: The following supporting information can be downloaded at: https://www.mdpi.com/article/10.3390/min13050646/s1, Table S1: The major oxide composition of light green and dark green glauconite pellets from the green shale facies of the Valia mine section, reported as EPMA point-counting data; Table S2: The major oxide composition of dark green pellets (glauconite) and the bioclast infillings (chamosite) and the brown pellets (chamosite) from the green shale facies of the Vastan mine section, reported as EPMA point-counting data; Table S3: The major oxide composition of spherulites of the spherulitic mudstone facies of the Valia mine section, reported as EPMA point-counting data.

Author Contributions: Conceptualization, S.B. and T.R.C.; methodology, S.B. and T.R.C.; software, T.R.C., P.S. and A.C.; validation, S.B. and T.R.C.; formal analysis, T.R.C., P.S. and A.C.; investigation, T.R.C., P.S. and A.C.; resources, S.B.; data curation, S.B. and T.R.C.; writing—original draft preparation, S.B. and T.R.C.; writing—review and editing, S.B. and T.R.C.; visualization, T.R.C. and P.S.; supervision, S.B.; project administration, S.B.; funding acquisition, S.B. All authors have read and agreed to the published version of the manuscript.

Funding: Department of Science and Technology (DST), India, provided a grant (INT/RUS/RFBR/390) to S.B. for analysis related to this research. T.R.C. received Post-Doctoral funding from IIT Bombay through the Institute of Eminence grant. P.S. is thankful to Council of Scientific Research, India (CSIR) for fellowship.

Data Availability Statement: Not Applicable.

Acknowledgments: Authors are thankful to IIT Bombay for the infrastructure support.

Conflicts of Interest: The authors declare no conflict of interest.

Abbreviations

The following abbreviations are used in this manuscript:

PETM	Paleocene Eocene Thermal Maximum
ETM 2	Eocene Thermal Maximum 2
SBZ	Shallow Benthic Zone
XRD	X-Ray Diffraction
EPMA	Electron Probe Micro Analyzer
A.S.T.M.	American Society for Testing and Materials

References

1. Odin, G.S.; Matter, A. De Glauconiarum Origine. *Sedimentology* **1981**, *28*. [CrossRef]
2. Amorosi, A.; Sammartino, I.; Tateo, F. Evolution Patterns of Glaucony Maturity: A Mineralogical and Geochemical Approach. *Deep. Res. Part II Top. Stud. Oceanogr.* **2007**, *54*, 1364–1374. [CrossRef]
3. López-Quirós, A.; Lobo, F.J.; Mendes, I.; Nieto, F. Holocene Glaucony from the Guadiana Shelf, Northern Gulf of Cadiz (SW Iberia): New Genetic Insights in a Sequence Stratigraphy Context. *Miner.* **2023**, *13*, 177. [CrossRef]
4. Clauer, N.; Keppens, E.; Stille, P. Sr Isotopic Constraints on the Process of Glauconitization. *Geology* **1992**, *20*, 133–136. [CrossRef]
5. Baldermann, A.; Dietzel, M.; Mavromatis, V.; Mittermayr, F.; Warr, L.N.; Wemmer, K. The Role of Fe on the Formation and Diagenesis of Interstratified Glauconite-Smectite and Illite-Smectite: A Case Study of Lower Cretaceous Shallow-Water Carbonates. *Chem. Geol.* **2017**, *453*, 21–34. [CrossRef]
6. Banerjee, S.; Bansal, U.; Vilas Thorat, A. A Review on Palaeogeographic Implications and Temporal Variation in Glaucony Composition. *J. Palaeogeogr.* **2016**, *5*, 43–71. [CrossRef]
7. Banerjee, S.; Choudhury, T.R.; Saraswati, P.K.; Khanolkar, S. The Formation of Authigenic Deposits during Paleogene Warm Climatic Intervals: A Review. *J. Palaeogeogr.* **2020**, *9*, 27.
8. Van Houten, F.B.; Bhattacharyya, D.P. Phanerozoic Oolitic Ironstones—Geologic Record and Facies Model. *Annu. Rev. Earth Planet. Sci.* **1982**, *10*, 441–457. [CrossRef]
9. Van Houten, F.B.; Purucker, M.E. Glauconitic Peloids and Chamositic Ooids—Favorable Factors, Constraints, and Problems. *Earth Sci. Rev.* **1984**, *20*, 211–243. [CrossRef]
10. Tang, D.; Shi, X.; Jiang, G.; Zhou, X.; Shi, Q. Ferruginous Seawater Facilitates the Transformation of Glauconite to Chamosite: An Example from the Mesoproterozoic Xiamaling Formation of North China. *Am. Mineral.* **2017**, *102*. [CrossRef]
11. Dasgupta, S.; Chaudhuri, A.K.; Fukuoka, M. Compositional Characteristics of Glauconitic Alterations of K-Feldspar from India and Their Implications. *J. Sediment. Res.* **1990**, *60*, 277–281. [CrossRef]
12. Giresse, P. Quaternary Glauconitization on Gulf of Guinea, Glauconite Factory: Overview of and New Data on Tropical Atlantic Continental Shelves and Deep Slopes. *Minerals* **2022**, *12*, 908. [CrossRef]
13. Porrenga, D.H. Glauconite and Chamosite as Depth Indicators in the Marine Environment. *Mar. Geol.* **1967**, *5*, 495–501. [CrossRef]
14. Berner, R.A. A New Geochemical Classification of Sedimentary Environments. *J. Sediment. Res.* **1981**, *51*, 359–365. [CrossRef]
15. Young, T.P. Phanerozoic Ironstones: An Introduction and Review. *Geol. Soc. Spec. Publ.* **1989**, *46*. [CrossRef]
16. Bekker, A.; Planavsky, N.J.; Krapež, B.; Rasmussen, B.; Hofmann, A.; Slack, J.F.; Rouxel, O.J.; Konhauser, K.O. Iron Formations: Their Origins and Implications for Ancient Seawater Chemistry. *Treatise Geochem. Second. Ed.* **2014**, *9*, 561–628. [CrossRef]
17. Tounekti, A.; Boukhalfa, K.; Choudhury, T.R.; Soussi, M.; Banerjee, S. Global and Local Factors behind the Authigenesis of Fe-Silicates (Glauconite/Chamosite) in Miocene Strata of Northern Tunisia. *J. African Earth Sci.* **2021**, *184*, 104342. [CrossRef]
18. Rudmin, M.; Mazurov, A.; Banerjee, S. Origin of Ooidal Ironstones in Relation to Warming Events: Cretaceous-Eocene Bakchar Deposit, South-East Western Siberia. *Mar. Pet. Geol.* **2019**, *100*, 309–325. [CrossRef]
19. Amorosi, A. Glaucony and Sequence Stratigraphy; a Conceptual Framework of Distribution in Siliciclastic Sequences. *J. Sediment. Res.* **1995**, *65*, 419–425. [CrossRef]
20. Roy Choudhury, T.; Banerjee, S.; Khanolkar, S.; Saraswati, P.K.; Meena, S.S. Glauconite Authigenesis during the Onset of the Paleocene-Eocene Thermal Maximum: A Case Study from the Khuiala Formation in Jaisalmer Basin, India. *Palaeogeogr. Palaeoclimatol. Palaeoecol.* **2021**, *571*, 110388. [CrossRef]
21. Bansal, U.; Banerjee, S.; Pande, K.; Ruidas, D.K. Unusual Seawater Composition of the Late Cretaceous Tethys Imprinted in Glauconite of Narmada Basin, Central India. *Geol. Mag.* **2020**, *157*, 233–247. [CrossRef]
22. Wigley, R.; Compton, J.S. Oligocene to Holocene Glauconite–Phosphorite Grains from the Head of the Cape Canyon on the Western Margin of South Africa. *Deep Sea Res. Part II Top. Stud. Oceanogr.* **2007**, *54*, 1375–1395. [CrossRef]
23. Roy Choudhury, T.; Khanolkar, S.; Banerjee, S. Glauconite Authigenesis during the Warm Climatic Events of Paleogene: Case Studies from Shallow Marine Sections of Western India. *Glob. Planet. Chang.* **2022**, *214*, 103857. [CrossRef]
24. Isson, T.T.; Planavsky, N.J. Reverse Weathering as a Long-Term Stabilizer of Marine PH and Planetary Climate. *Nature* **2018**, *560*, 471–475. [CrossRef]

25. Baldermann, A.; Banerjee, S.; Czuppon, G.; Dietzel, M.; Farkaš, J.; Löhr, S.; Moser, U.; Scheiblhofer, E.; Wright, N.M.; Zack, T. Impact of Green Clay Authigenesis on Element Sequestration in Marine Settings. *Nat. Commun.* **2022**, *13*, 1527. [CrossRef]
26. Taylor, K.G.; Macquaker, J.H.S. Iron Minerals in Marine Sediments Record Chemical Environments. *Elements* **2011**, *7*, 113–118. [CrossRef]
27. Zachos, J.; Pagani, H.; Sloan, L.; Thomas, E.; Billups, K. Trends, Rhythms, and Aberrations in Global Climate 65 Ma to Present. *Science* **2001**, *292*, 686–693. [CrossRef]
28. Nicolo, M.J.; Dickens, G.R.; Hollis, C.J.; Zachos, J.C. Multiple Early Eocene Hyperthermals: Their Sedimentary Expression on the New Zealand Continental Margin and in the Deep Sea. *Geology* **2007**, *35*, 699–702. [CrossRef]
29. Clementz, M.; Bajpai, S.; Ravikant, V.; Thewissen, J.G.M.; Saravanan, N.; Singh, I.B.; Prasad, V. Early Eocene Warming Events and the Timing of Terrestrial Faunal Exchange between India and Asia. *Geology* **2011**, *39*, 15–18. [CrossRef]
30. Rudmin, M.; Banerjee, S.; Mazurov, A. Compositional Variation of Glauconites in Upper Cretaceous-Paleogene Sedimentary Iron-Ore Deposits in South-Eastern Western Siberia. *Sediment. Geol.* **2017**, *355*, 20–30. [CrossRef]
31. Sluijs, A.; Van Roij, L.; Harrington, G.J.; Schouten, S.; Sessa, J.A.; LeVay, L.J.; Reichart, G.-J.; Slomp, C.P. Warming, Euxinia and Sea Level Rise during the Paleocene–Eocene Thermal Maximum on the Gulf Coastal Plain : Implications for Ocean Oxygenation and Nutrient Cycling. *Clim. Past* **2014**, *10*, 1421–1439. [CrossRef]
32. Anwar, D.; Choudhary, A.K.; Saraswati, P.K. Strontium Isotope Stratigraphy of the Naredi Formation, Kutch Basin, India. *India Artic. J. Geol. Soc. India* **2013**, *1*, 298–306. [CrossRef]
33. Samanta, A.; Bera, M.K.; Ghosh, R.; Bera, S.; Filley, T.; Pande, K.; Rathore, S.S.; Rai, J.; Sarkar, A. Do the Large Carbon Isotopic Excursions in Terrestrial Organic Matter across Paleocene-Eocene Boundary in India Indicate Intensification of Tropical Precipitation? *Palaeogeogr. Palaeoclimatol. Palaeoecol.* **2013**, *387*, 91–103. [CrossRef]
34. Saraswati, P.K.; Khanolkar, S.; Raju, D.S.N.; Dutta, S.; Banerjee, S.; Wang, Y.; Liu, M. Foraminiferal Biostratigraphy of Lignite Mines of Kutch India: Age of Lignite Fossil Vertebrates. *J. Palaeogeogr.* **2014**, *3*, 90–98.
35. Khanolkar, S.; Saraswati, P.K. ECOLOGICAL RESPONSE OF SHALLOW-MARINE FORAMINIFERA TO EARLY EOCENE WARMING IN EQUATORIAL INDIA. *J. Foraminifer. Res.* **2015**, *45*, 293–304. [CrossRef]
36. Roy Choudhury, T.; Banerjee, S.; Khanolkar, S.; Meena, S.S. Paleoenvironmental Conditions during the Paleocene–Eocene Transition Imprinted within the Glauconitic Giral Member of the Barmer Basin, India. *Minerals* **2022**, *12*, 56. [CrossRef]
37. Kumar, S.; Das, S.; Bastia, R.; Ojha, K. Mineralogical and Morphological Characterization of Older Cambay Shale from North Cambay Basin, India: Implication for Shale Oil/Gas Development. *Mar. Pet. Geol.* **2018**, *97*, 339–354. [CrossRef]
38. Biswas, S.K. Regional Tectonic Framework, Structure and Evolution of the Western Marginal Basins of India. *Tectonophysics* **1987**, *135*, 307–327. [CrossRef]
39. Garg, R.; Ateequzzaman, K.; Prasad, V.; Tripathi, S.K.M.; Singh, I.B.; Jauhri, A.K.; Bajpai, S. Age-Diagnostic Dinoflagellate Cysts from the Lignite-Bearing Sediments of the Vastan Lignite Mine, Surat District, Gujarat, Western India. *J. Palaeontol. Soc. India* **2008**, *53*, 99–105.
40. Phaye, D.K.; Bhattacharya, B.; Chakrabarty, S. Heterogeneity Characterization from Sequence Stratigraphic Analysis of Paleocene-Early Eocene Cambay Shale Formation in Jambusar-Broach Area, Cambay Basin, India. *Mar. Pet. Geol.* **2021**, *128*, 104986. [CrossRef]
41. Pundaree, N.; Krishna, A.K.; Subramanyam, K.S.V.; Sawant, S.S.; Kavitha, S.; Kalpana, M.S.; Patil, D.J.; Dayal, A.M. Early Eocene Carbonaceous Shales of Tadkeshwar Formation, Cambay Basin, Gujarat, India: Geochemical Implications, Petrogenesis and Tectonics. *Mar. Pet. Geol.* **2015**, *68*, 258–268. [CrossRef]
42. Misra, A.A.; Maitra, A.; Sinha, N.; Dey, S.; Mahapatra, S. Syn- to Post-Rift Fault Evolution in a Failed Rift: A Reflection Seismic Study in Central Cambay Basin (Gujarat), India. *Int. J. Earth Sci.* **2019**, *108*, 1293–1316. [CrossRef]
43. Ganguli, S.S.; Sen, S. Investigation of Present-Day in-Situ Stresses and Pore Pressure in the South Cambay Basin, Western India: Implications for Drilling, Reservoir Development and Fault Reactivation. *Mar. Pet. Geol.* **2020**, *118*, 104422. [CrossRef]
44. Punekar, J.; Saraswati, P.K. Age of the Vastan Lignite in Context of Some Oldest Cenozoic Fossil Mammals from India. *J. Geol. Soc. India* **2010**, *76*, 63–68. [CrossRef]
45. Prasad, V.; Singh, I.B.; Bajpai, S.; Garg, R.; Thakur, B.; Singh, A.; Saravanan, N.; Kapur, V.V. Palynofacies and Sedimentology-Based High-Resolution Sequence Stratigraphy of the Lignite-Bearing Muddy Coastal Deposits (Early Eocene) in the Vastan Lignite Mine, Gulf of Cambay, India. *Facies* **2013**, *59*, 737–761. [CrossRef]
46. Khanolkar, S.; Sharma, J. Record of Early to Middle Eocene Paleoenvironmental Changes from Lignite Mines, Western India. *J. Micropalaeontol.* **2019**, *38*, 1–24. [CrossRef]
47. Samanta, A.; Sarkar, A.; Bera, M.K.; Rai, J.; Rathore, S.S. Late Paleocene-Early Eocene Carbon Isotope Stratigraphy from a near-Terrestrial Tropical Section and Antiquity of Indian Mammals. *J. Earth Syst. Sci.* **2013**, *122*, 163–171. [CrossRef]
48. El Albani, A.; Meunier, A.; Fürsich, F. Unusual Occurrence of Glauconite in a Shallow Lagoonal Environment (Lower Cretaceous, Northern Aquitaine Basin, SW France). *Terra Nov.* **2005**, *17*, 537–544. [CrossRef]
49. Baldermann, A.; Warr, L.N.; Grathoff, G.H.; Dietzel, M. The Rate and Mechanism of Deep-Sea Glauconite Formation at the Ivory Coast-Ghana Marginal Ridge. *Clays Clay Miner.* **2013**, *61*, 258–276. [CrossRef]
50. López-Quirós, A.; Sánchez-Navas, A.; Nieto, F.; Escutia, C. New Insights into the Nature of Glauconite. *Am. Mineral.* **2020**, *105*, 674–686. [CrossRef]

51. Thompson, G.R.; Hower, J. The Mineralogy of Glauconite. *Clays Clay Miner.* **1975**, *23*, 289–300. [CrossRef]
52. Bansal, U.; Banerjee, S.; Nagendra, R. Is the Rarity of Glauconite in Precambrian Bhima Basin in India Related to Its Chloritization? *Precambrian Res.* **2020**, *336*, 105509. [CrossRef]
53. Burst, J.F. Mineral Heterogeneity in "Glauconite" Pellets. *Am. Mineral.* **1958**, *43*, 481–497.
54. Hower, J. Some Factors Concerning the Nature and Origin of Glauconite. *Am. Mineral.* **1961**, *46*, 313–334.
55. Deb, S.P.; Fukuoka, M. Fe-Illites in a Proterozoic Deep Marine Slope Deposit in the Penganga Group of the Pranhita Godavari Valley: Their Origin and Environmental Significance. *J. Geol.* **1998**, *106*, 741–749. [CrossRef]
56. Odin, G.S.; Fullagar, P.D. Chapter C4 Geological Significance of the Glaucony Facies. *Dev. Sedimentol.* **1988**, *45*. [CrossRef]
57. Bansal, U.; Banerjee, S.; Pande, K.; Arora, A.; Meena, S.S. The Distinctive Compositional Evolution of Glauconite in the Cretaceous Ukra Hill Member (Kutch Basin, India) and Its Implications. *Mar. Pet. Geol.* **2017**, *82*, 97–117. [CrossRef]
58. Eder, V.G.; Martín-Algarra, A.; Sánchez-Navas, A.; Zanin, Y.N.; Zamirailova, A.G.; Lebedev, Y.N. Depositional Controls on Glaucony Texture and Composition, Upper Jurassic, West Siberian Basin. *Sedimentology* **2007**, *54*, 1365–1387. [CrossRef]
59. Jach, R.; Starzec, K. Glaucony from the Condensed Lower-Middle Jurassic Deposits of the Krizna Unit, Western Tatra Mountains, Poland. *Ann. Soc. Geol. Pol.* **2003**, *73*, 183–192.
60. Berg-Madsen, V. High-Alumina Glaucony from the Middle Cambrian of Oeland and Bornholm, Southern Baltoscandia. *J. Sediment. Res.* **1983**, *53*, 875–893. [CrossRef]
61. Skiba, M.; Maj-Szeliga, K.; Szymański, W.; Błachowski, A. Weathering of Glauconite in Soils of Temperate Climate as Exemplified by a Luvisol Profile from Góra Puławska, Poland. *Geoderma* **2014**, *235–236*, 212–226. [CrossRef]
62. Fanning, D.S.; Rabenhorst, M.C.; May, L.; Wagner, D.P. Oxidation State of Iron in Glauconite from Oxidized and Reduced Zones of Soil-Geologic Columns. *Clays Clay Miner.* **1989**, *37*, 59–64. [CrossRef]
63. Courbe, C.; Velde, B.; Meunier, A. Weathering of Glauconites: Reversal of the Glauconitization Process in a Soil Profile in Western France. *Clay Miner.* **1981**, *16*, 231–243. [CrossRef]
64. Giresse, P.; Odin, G.S. Nature Mineralogique et Origine Des Glauconies Du Plateau Continental Du Gabon et Du Congo. *Sedimentology* **1973**, *20*, 457–488. [CrossRef]
65. Andrade, G.R.P.; de Azevedo, A.C.; Cuadros, J.; Souza, V.S.; Furquim, S.A.C.; Kiyohara, P.K.; Vidal-Torrado, P. Transformation of Kaolinite into Smectite and Iron-Illite in Brazilian Mangrove Soils. *Soil Sci. Soc. Am. J.* **2014**, *78*, 655–672. [CrossRef]
66. Dai, S.; Chou, C.L. Occurrence and Origin of Minerals in a Chamosite-Bearing Coal of Late Permian Age, Zhaotong, Yunnan, China. *Am. Mineral.* **2007**, *92*, 1253–1261. [CrossRef]
67. Stonecipher, S.A. Genetic Characteristics of Glauconite and Siderite: Implications for the Origin of Ambiguos Isolated Marine Sandbodies. *SEPM Spec. Publ.* **1999**, *64*, 191–204.
68. Passey, S.R. The Habit and Origin of Siderite Spherules in the Eocene Coal-Bearing Prestfjall Formation, Faroe Islands. *Int. J. Coal Geol.* **2014**, *122*, 76–90. [CrossRef]
69. Mozley, P.S. Relation between Depositional Environment and the Elemental Composition of Early Diagenetic Siderite. *Geology* **1989**, *17*, 704–706. [CrossRef]
70. Serra-Kiel, J.; Hottinger, L.; Schaub, H.; Sirel, E.; Strougo, A.; Tambareau, Y.; Tosquella, J.; Zakrevskaya, E.; Caus, E.; Drobne, K.; et al. Larger Foraminiferal Biostratigraphy of the Tethyan Paleocene and Eocene. *Bull. la Société Géologique Fr.* **1998**, *169*, 281–299.
71. Stassen, P.; Thomas, E.; Speijer, R.P. Paleocene-Eocene Thermal Maximum Environmental Change in the New Jersey Coastal Plain: Benthic Foraminiferal Biotic Events. *Mar. Micropaleontol.* **2015**, *115*, 1–23. [CrossRef]
72. John, C.M.; Bohaty, S.M.; Zachos, J.C.; Sluijs, A.; Gibbs, S.; Brinkhuis, H.; Bralower, T.J. North American Continental Margin Records of the Paleocene-Eocene Thermal Maximum: Implications for Global Carbon and Hydrological Cycling. *Paleoceanography* **2008**, *23*, PA2217. [CrossRef]
73. Carmichael, M.J.; Inglis, G.N.; Badger, M.P.S.; Naafs, B.D.A.; Behrooz, L.; Remmelzwaal, S.; Monteiro, F.M.; Rohrssen, M.; Farnsworth, A.; Buss, H.L.; et al. Hydrological and Associated Biogeochemical Consequences of Rapid Global Warming during the Paleocene-Eocene Thermal Maximum. *Glob. Planet. Chang.* **2017**, *157*, 114–138. [CrossRef]
74. Bolle, M.-P.; Adatte, T. Palaeocene- Early Eocene Climatic Evolution in the Tethyan Realm: Clay Mineral Evidence. *Clay Miner.* **2001**, *36*, 249–261. [CrossRef]
75. Bolle, M.P.; Tantawy, A.A.; Pardo, A.; Adatte, T.; Burns, S.; Kassab, A. Climatic and Environmental Changes Documented in the Upper Paleocene to Lower Eocene of Egypt. *Eclogae Geol. Helv.* **2000**, *93*, 33–51.
76. Rudmin, M.; Banerjee, S.; Abdullayev, E.; Ruban, A.; Filimonenko, E.; Lyapina, E.; Kashapov, R.; Mazurov, A. Ooidal Ironstones in the Meso-Cenozoic Sequences in Western Siberia: Assessment of Formation Processes and Relationship with Regional and Global Earth Processes. *J. Palaeogeogr.* **2020**, *9*, 1–21. [CrossRef]
77. Todd, S.E.; Pufahl, P.K.; Murphy, J.B.; Taylor, K.G. Sedimentology and Oceanography of Early Ordovician Ironstone, Bell Island, Newfoundland: Ferruginous Seawater and Upwelling in the Rheic Ocean. *Sediment. Geol.* **2019**, *379*, 1–15. [CrossRef]
78. Kharkwal, A.D. Glauconite in the Subathu Beds (Eocene) of the Simla Hills of India. *Nature* **1966**, *211*, 615–616. [CrossRef]
79. Chowns, T.M. Depositional Environment of the Cleveland Ironstone Series. *Nature* **1966**, *211*, 1286–1287. [CrossRef]
80. Choi, K.S.; Khim, B.K.; Woo, K.S. Spherulitic Siderites in the Holocene Coastal Deposits of Korea (Eastern Yellow Sea): Elemental and Isotopic Composition and Depositional Environment. *Mar. Geol.* **2003**, *202*, 17–31. [CrossRef]

81. Lim, D.I.; Jung, H.S.; Yang, S.Y.; Yoo, H.S. Sequential Growth of Early Diagenetic Freshwater Siderites in the Holocene Coastal Deposits, Korea. *Sediment. Geol.* **2004**, *169*, 107–120. [CrossRef]
82. Postma, D. Pyrite and Siderite Formation in Brackish and Freshwater Swamp Sediments. *Am. J. Sci.* **1982**, *282*, 1151–1183. [CrossRef]

Disclaimer/Publisher's Note: The statements, opinions and data contained in all publications are solely those of the individual author(s) and contributor(s) and not of MDPI and/or the editor(s). MDPI and/or the editor(s) disclaim responsibility for any injury to people or property resulting from any ideas, methods, instructions or products referred to in the content.